

Decoupling the role of inertia, friction and cohesion in dense granular avalanche pressure build-up on obstacles

M. L. Kyburz^{1,2*}, B. Sovilla¹, J. Gaume^{1,3}, C. Ancey²

¹WSL Institute for Snow and Avalanche Research SLF, Davos, Switzerland

²Environmental Hydraulics Laboratory, Swiss Federal Institute of Technology, Lausanne, Switzerland

³Snow and Avalanche Simulation Laboratory SLAB, Swiss Federal Institute of Technology, Lausanne, Switzerland

Key Points:

- We simulate impact pressure of cohesive granular flows on obstacles with the Discrete Element Method
- The impact pressure on structures consists of the inertial, frictional and cohesive contributions
- The strength of force chains and size of the mobilized domain govern the pressure build-up

*Current address,

Michael L. Kyburz

WSL Institute for Snow and Avalanche Research SLF

CH-7260 Davos Dorf

Corresponding author: Michael L. Kyburz, kyburz@slf.ch

Abstract

Understanding the physical processes involved in snow avalanche-obstacle interaction is essential to be able to estimate the pressure exerted on structures. Although avalanche impact pressure has been measured in full-scale for decades, the underlying physical principles are still elusive. Previous studies suggest that pressure is increased due to the formation of an influenced flow region around the structure, the mobilized domain, which varies in size depending on snow properties, such as snow cohesion. Here, we aim to better understand how cohesion, friction, velocity and their interplay affect avalanche pressure build-up on structures. This is achieved by simulating the avalanche-obstacle interaction with a newly developed numerical model based on the Discrete Element Method, using a cohesive bond contact law. The relevance of the model is tested by comparing simulated impact pressures with full-scale measurements from the Vallée de la Sionne experimental site. Our results show that at the macro-scale, impact pressure consists of the inertial, frictional and cohesive contributions. The inertial and frictional contributions arise due to the existence, shape and dimension of the mobilized domain. The cohesive contribution increases the particle contact forces inside the domain, leading up to a doubling of the pressure. Based on these physical processes, we propose a novel scaling law to reduce the problem of calculating the pressure induced by cohesive flows, to the calculation of cohesion-less flows. These findings enhance our understanding of the interaction of cohesive granular flows, such as snow avalanches, and structures at the micro and macro-scale.

1 Introduction

How a flow behaves past an obstacle is a problem of fundamental importance in fluid mechanics. A related problem that has attracted considerable attention is the force exerted by the flow on an obstacle. For Newtonian fluids, two processes generate a force on an obstacle: the fluid pressure and the viscous forces. There is no general expression that holds for all flow configurations, but for some flows, analytical expressions have been derived. These concepts, however, can not always be extrapolated successfully for non-Newtonian fluids like snow avalanches (*Ancey & Bain, 2015*).

Indeed, snow avalanche pressure on obstacles is generally assessed by referring to two limiting cases. When the velocity is high, the impact pressure is calculated in a manner analogous to an inviscid fluid, where pressure is proportional to fluid density times

the velocity squared ($p \propto \rho \cdot v^2$) (*Salm, 1966; Burkard et al., 1990; Sovilla et al., 2008a; Baroudi & Thibert, 2009*). If the velocity is low, snow avalanches are often approximated as cohesive granular flows (*Bartelt & McArdell, 2009; Steinkogler et al., 2015*), and are considered to be analogous to quasi-static granular flows, where impact pressure is proportional to gravity, density and the immersion height of the obstacle in the medium ($p \propto \rho \cdot g \cdot h$) (*Wieghardt, 1975; Albert et al., 1999; Sovilla et al., 2010*).

Often the Froude Number (equation 1) is used to classify these two flow regimes. The case of fast avalanches is referred to as the inertial regime (supercritical, $Fr > 1$), and to the case of slow avalanches as the gravitational regime (subcritical, $Fr < 1$) (*Mellor, 1968*).

$$Fr = v / \sqrt{g \cdot h} \quad (1)$$

This is, however, a very coarse distinction as *Köhler et al. (2018a)* have recently shown that even for the same topography, the flow regimes can be manifold. It is assumed that snow properties, which are mechanically and thermodynamically very sensitive, are a main contributor to this diversity of flow behaviors as well as an important influence on avalanche-obstacle interaction behavior, which is not yet fully understood (*Köhler et al., 2018b; Steinkogler et al., 2015*).

The problem of snow avalanche impact pressure has been investigated for some decades in full-scale experiments (*Gauer & Kristensen, 2016; Thibert et al., 2015; Sovilla et al., 2008b*) and small-scale chute experiments (*Salm, 1964; Moriguchi et al., 2009; Hauks-son et al., 2007*). Full-scale avalanche measurements (*Sovilla et al., 2010, 2016*) and studies on granular materials (*Faug, 2015; Favier et al., 2013*) indicate concurrently that the formation of force chains and cohesion, as well as the formation of a mobilized domain, where the flow is influenced by the presence of an obstacle, may increase the impact pressure of slow avalanches or granular flows in general. However, as *Faug (2015)* points out, further investigation on the size and shape of the mobilized domain, as well as the corresponding pressure on the obstacle, is needed to bridge the gap between processes at the micro-scale and the macroscopic force experienced by the obstacle.

The evidence that snow avalanches have a granular nature (*Salm, 1966; Mellor, 1968*) has prompted the idea to explore the interaction between avalanches and structures using the Discrete Element Method (DEM). While multiple studies investigate the force exerted by a cohesion-less granular material on an obstacle using DEM (*Chanut*

et al., 2009; Calvetti et al., 2017; Teufelsbauer et al., 2011), only few have considered that of a cohesive material (e.g. Favier et al., 2013).

Hence, here we aim to identify which processes are involved in avalanche-obstacle interaction and assess how they contribute to pressure build-up on structures for a large range of Froude numbers and cohesion values. More specifically, we aim to clarify how cohesion influences the flow, the mobilized domain and the impact pressure.

In this paper we tackle this issue by developing a new numerical model to reconstruct the processes occurring when an avalanche interacts with an obstacle using DEM with a cohesive bond contact model. We take advantage of the data acquired at the “Vallée de la Sionne” (VdS) field site, in Valais, Switzerland (Ammann, 1999) to constrain the model parameters and test the model relevance. To compare simulated and measured impact pressures, we implement the geometry of a 20 m high measurement pylon, where most of the measurements are taken, and use two commonly observed avalanche scenarios. In VdS, gravitational avalanches are often characterized by slowly moving snow (Table 1) with constant velocity over the whole flow height, while the inertial regime is mostly typical of fast moving snow (Table 1), which often exhibits a vertical shear velocity profile (Sovilla et al., 2008a; Kern et al., 2009).

By varying the cohesion and the velocity of the granular flow and analyzing the simulated impact pressure in each configuration, we identify different impact pressure contributions, especially the contribution of cohesion. In addition, we investigate the structure of the simulated flow around the obstacle at the particle level to identify the processes involved in the avalanche-obstacle interaction and to better interpret the measured and simulated pressures which arise at the obstacle. Finally, we back calculate the range of cohesion from four gravitational snow avalanches measured at VdS, to revisit the relevance of the cohesion values used in the simulations for real avalanches.

2 Materials and Methods

This section describes the method used to model snow avalanche pressure on obstacles. In the first part, we define the test case and present experimental data which we use for the comparison with the simulations. The second part outlines how we model snow with DEM. In the third section, we present the model setup. Finally, we summarize the most important parameters used in the simulations. This paper’s supporting in-

formation presents the details of the implementation of the numerical Discrete Element Method, the contact model, as well as the model setup and procedure.

2.1 Experimental data and test case

Over the past 20 years, a large set of full-scale measurements has been collected at VdlS. Therefore, we choose the measurement data from this site as the test case to model avalanche flow and pressure in the present study. Among many other quantities, avalanche pressure and velocity are measured on a 20 m high pylon-like steel structure (Sovilla *et al.*, 2010). The pylon is located on a flat slope beneath two couloirs, where avalanches releasing from a 1.5 km wide area converge (Ammann, 1999). Here, we use the term pressure to refer to the measured or simulated impact pressure on the obstacle, if not mentioned otherwise. At the pylon, the pressure is measured at the front of six cylinders distributed with 1 m vertical spacing (Sovilla *et al.*, 2014). The velocity of the incoming flow is measured at the face of a wedge attached to the front of the pylon (Kern *et al.*, 2010). These point measurements at the pylon are complemented by radar measurements, which provide information on the flow regime along the ~ 2.5 km long flow path (Köhler *et al.*, 2018a).

Based on radar measurement data from VdlS, avalanche flows have been reclassified recently into seven categories (Köhler *et al.*, 2018a). This highlights the complexity of avalanche flows, which also strongly depend on the specific terrain and the snow properties. In this study however, we limit ourselves to two flow types, which are often observed at the VdlS test site, namely, the inertial shear flow and the gravitational plug flow regimes.

Full-scale experiments have demonstrated, that in the inertial flow regime, which is mostly typical of fast and cold avalanches, the pressure is proportional to velocity squared. Throughout this paper, we refer to cold or warm avalanches as avalanches with prevailing snow temperatures below or above -1°C , respectively. Previous research suggests that snow undergoes dramatic changes at this temperature, which consequently influences avalanche flow dynamics (Steinkogler *et al.*, 2015; Köhler *et al.*, 2018a; Fischer *et al.*, 2018). The dense flows of inertial avalanches at VdlS rarely exceed a flow height of $h = 2.5$ m and often exhibit a sheared velocity profile (Kern *et al.*, 2009). Typical velocities of the inertial dense flow at VdlS range from 10 m/s to 30 m/s (Sovilla *et al.*, 2008a).

The gravitational regime is often observed for warm snow avalanches and features a linear pressure variation with flow depth. A typical gravitational plug flow avalanche flows at very low velocities up to a maximum of approximately 10 m/s, at the pylon location. At the VdIS test site these avalanches can build up maximum flow heights of 5 – 7 m and exert pressures in the range of 100 – 500 kPa (*Sovilla et al.*, 2016). However, at VdIS, the peak flow heights are rarely maintained over longer time spans, but decrease with time. Heights of $h \lesssim 4$ m are more common for this kind of flow.

2.2 Modeling snow using the Discrete Element Method

Our model is implemented within the framework of Itasca’s commercial PFC software. This software implements the DEM method based on the soft-contact algorithm (*Cundall & Strack*, 1979) for interacting discrete particles.

Because of limited computational power, the number of snow crystals involved in large avalanches is prohibitive to be resolved as individual discrete elements in the model. Therefore, we consider the discrete particles to correspond to small snow agglomerates rather than individual ice crystals. Hence, the radius of the particles in the simulations are normally distributed within the interval $32 \text{ mm} \leq r_p \leq 48 \text{ mm}$ corresponding to a mean value of $r_p = 40 \text{ mm}$. According to field surveys, this corresponds to an intermediate granule size (*Bartelt & McArdell*, 2009; *Sovilla et al.*, 2008a; *Steinkogler et al.*, 2015). Because snow particles are not resolved individually, the material properties of the discrete elements in the model must correspond to the macroscopic properties of the snow granules rather than the ice properties at the crystal level.

In DEM, the material’s characteristics are not only influenced by the particles’ properties. The dynamical behavior is primarily governed by the contact model, which comes into play whenever two particles interact with each other. A suitable contact law is therefore of prime importance to mimic the flowing snow in an avalanche. In the present work, a parallel bond contact model (*Potyondy & Cundall*, 2004) is used to model the mechanical behavior of snow. The model consists of two components: (1) a classical linear viscoelastic component consisting of a spring and a dashpot in the normal direction and a spring and a coulomb friction limit in the tangential direction, as well as (2) an elastic-brittle cohesive bond in parallel to the linear component. The bond models the sintering and therefore cohesion of the real snow. Mechanically it acts like a beam connecting the particles and can sustain normal and shear forces as well as bending and torsional

loads. Similar to the sintering in snow, also in our simulations we allow for new bonds to form if a new contact occurs between two unbonded particles. Because the bond is in parallel to the linear component, the cohesion-less behavior is conserved in any case, such as after bond breakage before a new bond forms.

2.3 Modeling the interaction of the avalanche flow and structures

In order to perform a systematic study of the influence of velocity and cohesion on impact pressure, we aim to impose the flow of the granular material independently from the particle and contact properties in the DEM model. Therefore, we propose a setup which enforces the flowing granular material (e.g. snow) to match a specific vertical velocity profile.

To achieve this, we isolate a finite volume of particles around the obstacle. The computational domain is 28 m high (z direction) and is confined with a wall at the bottom. This bottom wall mimics the gliding surface on which the avalanche flows. Transverse to the flow (y direction), the domain is 7 m wide and is limited by a periodic boundary condition. In the streamwise direction (x direction), the domain is 10 m long and is limited by pushing walls, segmented in height (Figure 1). By moving the wall segments at different speeds at different heights, we can impose the velocity magnitude and profile to the particle volume. In this way the velocity past the obstacle can be controlled while also accounting for effects such as basal friction and shear dilatancy.

For the simulations, we use idealized plug and shear velocity profiles. In the gravitational plug flow, we impose a constant velocity over the whole flow height (Figure 1 a). In the inertial shear flow, the velocity increases linearly from the bottom to the free surface of the granular flow (Figure 1 b). Ranges for cohesion and velocity, velocity profiles and flow heights are given in Table 1.

Gravity points in the negative z direction. While the average slope in the region of the VdS pylon is approximately 20° , this approximation can be justified in the context of our test case because the terrain up to 10 m upstream of the pylon is nearly flat.

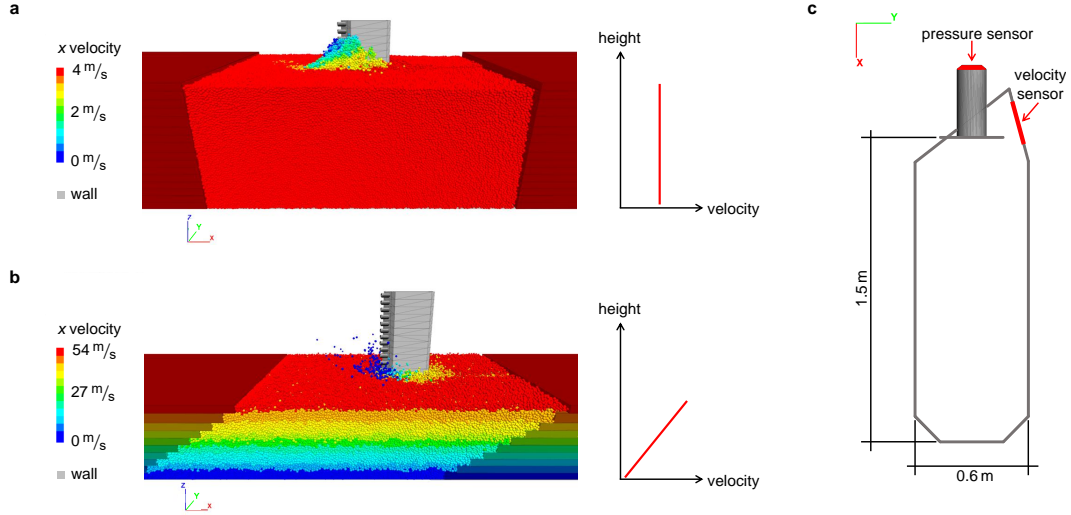


Figure 1. Panels a and b show DEM simulations of a plug flow and a shear flow and the corresponding velocity profile, respectively. The pushing walls and the discrete elements are colored according to the velocity in the streamwise direction. The pushing walls and the static obstacle are shaded in gray. Panel c shows the cross section of the pylon with the location of the pressure and velocity sensors.

This DEM model is tested by comparing the simulation results to full-scale measurements from VdIS. To allow for direct comparison between simulations and measurements, the geometry of the obstacle in the simulation is similar to the shape of the steel pylon at VdIS as depicted in Figure 1 c. Pressure and velocity in the simulations are sampled at the same locations, which are highlighted in red in Figure 1 c, and at the same temporal frequency as in VdIS.

The simulated velocity sampled at the side of the structure is only used for the comparison of the simulated and the experimentally measured impact pressure in Figure 2 and 3. Otherwise, we always use the imposed velocity at the wall. The simulated impact pressure is determined by summing up the face-normal component of all contact forces acting on the measurement surface and dividing it by the sensor surface area.

To compare simulations, we always use a representative value of contact force, velocity at the pylon, imposed velocity, confining pressure and impact pressure, which corresponds to the value at mid flow depth.

2.4 Model parameters

While it is notoriously difficult to measure the mechanical properties of snow due to its heterogeneity (*Gerling et al.*, 2017; *Gaume et al.*, 2015a), even less is known about the mechanical properties of flowing snow in avalanches. As mentioned earlier, this applies particularly for cohesion, which is of central interest in the present study. Thus, most of the parameters and material properties applied in the simulations of this study are estimated rather than rigorously measured or calibrated with values within typical ranges as used and suggested by other authors for snow.

As mentioned in section 2.1, gravitational and inertial avalanches have different snow and flow properties. In the present article we want to focus on the influence of velocity and cohesion on the impact pressure. Hence, in our parametric study we only vary the cohesion as well as the flow height and the velocity according to the two flow regimes given in Table 1. Parameters such as the friction coefficient $\mu = 0.5$ (*Steinkogler et al.*, 2015; *Gaume et al.*, 2015b, 2018), Young’s modulus E , particle radius r_p (section 2.2) and particle density $\rho_p = 500 \text{ kg/m}^3$ of a single discrete element are constant in all simulations. In contrast to ρ_p , the bulk density ρ_b is the volumetric average density including voids between particles in a spherical control volume with a radius of $5.0 \cdot r_p$. Hence, ρ_b varies as a result of cohesion and shear rates, ranging from 370 kg/m^3 to 430 kg/m^3 in the gravitational plug flows and from 300 kg/m^3 to 365 kg/m^3 in the inertial shear flows. The ranges of these bulk densities agree well with the values from field and experimental studies (*Platzner et al.*, 2007; *Steinkogler et al.*, 2015; *Bartelt & McArdeell*, 2009).

For the particles’ Young’s modulus, we use a value of $E = 10^5 \text{ Pa}$ in all simulations, which is in the lower range of the values used by *Gaume et al.* (2015b) for modeling snow slabs and in the range of reported values from the literature (*Shapiro et al.*, 1997; *Gerling et al.*, 2017; *Scapozza*, 2004). For Young’s modulus of the cohesive bond, we use the same value as for the particles. The cohesive strength of the bond is set to $\sigma_{coh.less} = 0 \text{ Pa}$ for cohesion-less simulations and varied between $0 \text{ kPa} < \sigma_{coh} \leq 20 \text{ kPa}$ otherwise. The upper limit corresponds roughly to the values reported by *Shapiro et al.* (1997) for snow with densities from 320 kg/m^3 to 420 kg/m^3 and is the same range as used by *Gaume et al.* (2015b). In the present study we use the local Bond number (equation 2) instead of σ_{coh} to analyze the influence of the cohesive strength.

$$Bo = \sigma_{coh}/p_{conf} \quad (2)$$

This dimensionless number is the re-scaled cohesion, defined as the cohesive strength divided by the confining pressure p_{conf} (Roy *et al.*, 2017), where the confining pressure is the vertical component of the local stress tensor $p_{conf} \equiv \sigma_{zz}$.

The parameters discussed here are summarized in Table 1.

Table 1. Parameters for the DEM simulations in the gravitational and inertial regime

Parameter	Symbol	Unit	Gravitational plug flow	Inertial shear flow
Particle density	ρ_p	kg/m ³	500	500
Bulk density*	ρ_b	kg/m ³	370 – 430	300 – 366
Young’s modulus	E	Pa	10^5	10^5
Cohesive strength	σ_{coh}	Pa	$0.0 - 2.0 \cdot 10^4$	$0.0 - 2.0 \cdot 10^4$
Friction coefficient	μ	–	0.5	0.5
Particle radius	r_p	mm	40 ± 8	40 ± 8
Depth-averaged velocity	v	m/s	2 – 8	15 – 40
Flow height	h	m	4.0	2.5

* The bulk density is not an input parameter, but is mentioned here for illustrative reasons.

3 Results

The following section presents the results of our study on the influence of velocity and cohesion on the avalanche pressure on the VdlS pylon. The results are divided into four parts. In the first step, we compare the simulated impact pressure to full-scale measurements from VdlS to test whether the model proposed in section 2 is able to reproduce field measurements. Secondly, we show the results of the parametric study, where we vary velocity and cohesion in our simulation. There we analyze how impact pressure is influenced by changes in these two variables. In the third step, we analyse the flow around the obstacle at the micro-scale to better interpret and understand the influence of velocity and cohesion on the impact pressure. In the fourth step, we analyze the range of cohesion, the pressures and pressure fluctuations in gravitational avalanches with regard to the results from the previous sections.

3.1 Comparison of DEM simulations with full-scale measurements

For the comparison of simulations with measurements, we select examples of field measurements of a gravitational plug flow and an inertial shear flow from the VdIS archive, respectively. The simulations start by imposing a velocity profile using the pushing walls. The resulting velocity profile at the pylon, which is different from the imposed one, is then compared to the measured velocity profile. The other parameters in the simulations are kept constant as described in Table 1. The only free parameter is the cohesion, which to date can not be measured in the experiments and can only be estimated for the simulations (section 2.4).

In the case of the gravitational flow, we select measurements performed in a warm avalanche (archive number # 20103003 in the VdIS database), which released naturally on 30 December 2009. From these measurements we extract a short time sequence in the order of 0.5 s to obtain the pressure and velocity profile. In Figure 2 a these measurements are compared to a simulation with an imposed plug velocity profile of 10 m/s, a flow height of 4 m and a cohesive strength of $\sigma_{coh} = 15.6$ kPa. The chosen cohesion is high considering the range of σ_{coh} given in Table 1, as expected from a typical warm plug flow avalanche.

The plug velocity profile imposed at the walls results in the red velocity profile of ~ 8 m/s at the pylon (Figure 2 a, left panel). Above a flow height of 4 m, the velocity decreases, as observed in the measurements. The qualitative trend of the simulated pressure profile agrees with the measured pressure profile, which increases linearly with the flow depth (Figure 2 a, right panel). However, the simulated pressure increases at a slightly higher rate near the free surface of the flow, and at a slightly lower rate below ~ 3.5 m than in the real-scale experiment.

In the case of the inertial shear flow we choose the measurement of avalanche # 20173032, which was released artificially on 08 March 2017. In Figure 2 b these measurements are compared to a simulation with an imposed shear velocity profile of 0 – 20 m/s, a flow height of 2.5 m and a cohesive strength of $\sigma_{coh} = 1.25$ kPa. As it would be expected for an inertial shear flow, the selected cohesion is considerably lower than the one of the gravitational plug flow.

The shear velocity profile imposed at the walls results in the red velocity profile at the pylon shown in Figure 2 b, left panel. The simulated velocity profile shows a good agreement with the measurements, with the exception of the lower layers in the flow, at a flow height of ~ 1.0 m. However, this small difference does not seem to affect the pres-

279 sure profiles in Figure 2 b, right panel, which shows a very good agreement between the
 280 simulated and measured pressures.

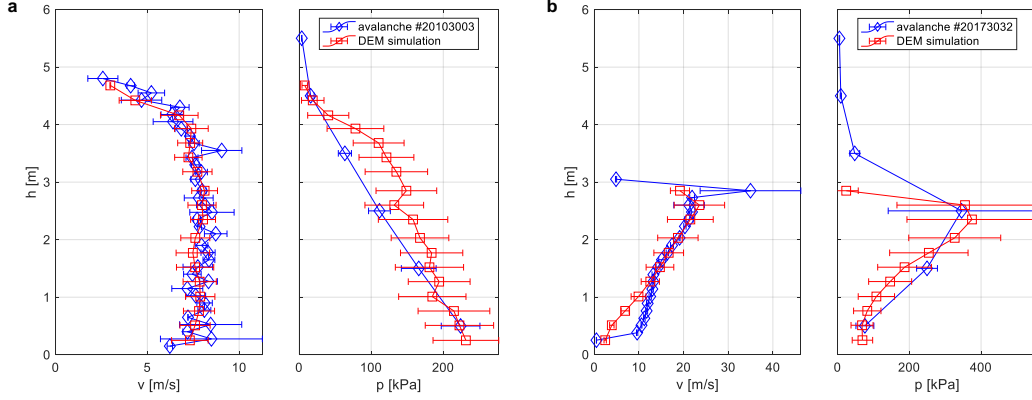


Figure 2. Panels a and b show the comparison of simulated (red squares) and measured (blue diamonds) velocity and pressure profiles for an example of a plug flow and a shear flow, respectively. The error bars indicate the standard deviation from the mean value of the pressure or velocity. The interpolating lines between the data points are only a visual aid.

281 In order to test the relevance of our model in simulating the correct pressure for
 282 a larger range of velocities and cohesions, we vary the cohesive strength and velocity in
 283 our simulations according to the ranges given in Table 1.

284 In Figure 3, we compare the simulated impact pressures to full-scale measurements
 285 of two avalanches (# 7226, # 6236, published by *Sovilla et al. (2008a)*). We can see that
 286 the simulated and measured impact pressure values in Figure 3 show good agreement over
 287 a wide range of avalanche velocities. For low velocities up to 10 m/s, the scatter of the
 288 simulated data is in the same range as the scatter of the measured data. The large scat-
 289 ter of the measurements for velocities higher than 10 m/s is very likely to be caused by
 290 the variability of the snow properties in the avalanches (*Köhler et al., 2018b*). The scat-
 291 ter in the simulations is smaller because many snow properties are kept constant (Ta-
 292 ble 1). Specifically, the scatter of the simulated impact pressure is caused only by the vari-
 293 ation of cohesion, flow height or imposed velocity.

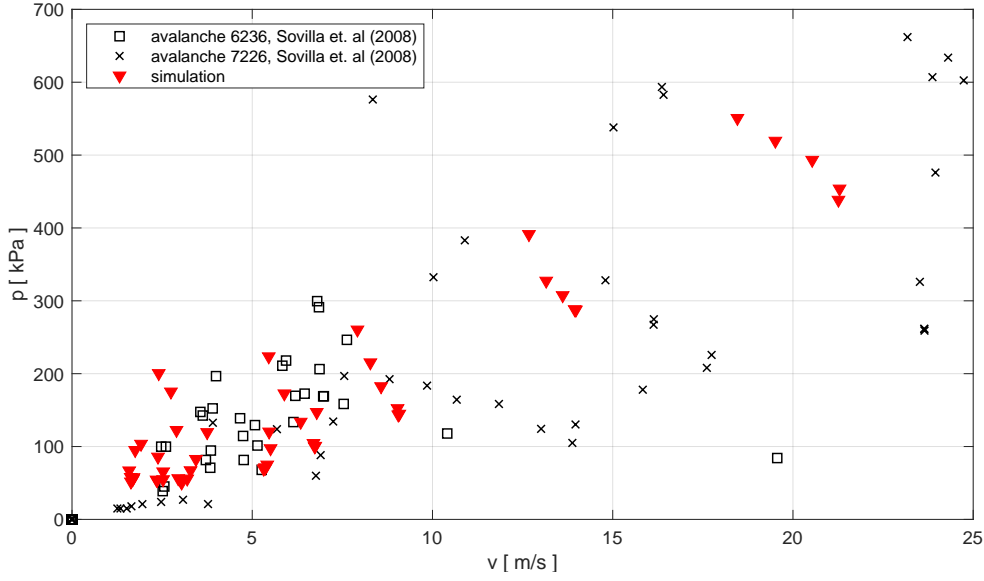


Figure 3. Comparison of simulated (red triangles) and measured (black symbols) impact pressure versus velocity.

3.2 Influence of velocity and cohesion on impact pressure

In this section we analyze the influence of velocity and cohesion on impact pressure. For this purpose, we vary both quantities systematically in the ranges given in Table 1.

Figure 4a shows the simulated impact pressures p on the obstacle plotted over a range of velocities. Here we plot the impact pressure of cohesion-less simulations connected by the dashed black line, and the simulations with the strongest cohesion $\sigma_{coh} = 20$ kPa connected by the dash-dotted black line. We observe that the dashed and the dash-dotted line only vary little at slow velocities under 4 m/s, as found earlier for cohesion-less granular materials (*Albert et al.*, 1999; *Wieghardt*, 1975). For velocities higher than 4 m/s, the pressure increases gradually, for the cohesive and the cohesion-less case.

In this graph we identify three pressure contributions which are illustrated by the black lines in Figure 4a, and the colored areas in the inset thereof. We define the first impact pressure contribution as the inertial contribution, which is proportional to velocity squared $p \propto v^2 \cdot \rho/2$ (*Salm*, 1966), similarly to the hydrodynamic impact pressure of inviscid fluids. This contribution is visualized in Figure 4a by the blue area in the inset and the black solid line, which is calculated using a constant density $\rho = 300$ kg/m³ as suggested by *Burkard et al.* (1990). The slope of the the cohesion-less pressure curve

reaches a maximum of 1.9 between 30 m/s and 40 m/s, very close to the theoretical value 2.0 given by the v^2 proportionality. Hence, Figure 4 a shows, that this is only a good approximation for the pressure of fast flows in the inertial regime ($v \gtrsim 20$ m/s).

For flows where $v \leq 15$ m/s, we observe that the lowest simulated pressures, which are connected by the dashed black line and correspond to cohesion-less simulations, are well above the solid black line. Hence, we define the second contribution as the pressure difference between the dashed and the solid black line at a constant velocity, and refer to it as the frictional pressure contribution. It is highlighted with the yellow area in the inset. The frictional contribution arises due to the granular nature of the flow which we inherently simulate with DEM, in contrast to the flow of a Newtonian fluid. Figure 4 a shows that this contribution is mostly relevant for the gravitational flow ($2 \leq v \leq 8$ m/s).

The third pressure contribution is the cohesive contribution, visualized with the red area in the inset. We define it as the pressure difference between the dash-dotted and the dashed black line at a constant velocity. Thus, the cohesive contribution is the difference between impact pressure of a cohesive and a cohesion-less simulation and is solely caused by the presence of cohesion. From Figure 4 a we find that, for the maximum cohesion $\sigma_{coh} = 20$ kPa, the maximum pressure increase due to cohesion is 70 % at 3 m/s and 14 % at 40 m/s, respectively. Hence, similarly to the frictional contribution also the cohesive contribution is more relevant for gravitational flows than for inertial flows.

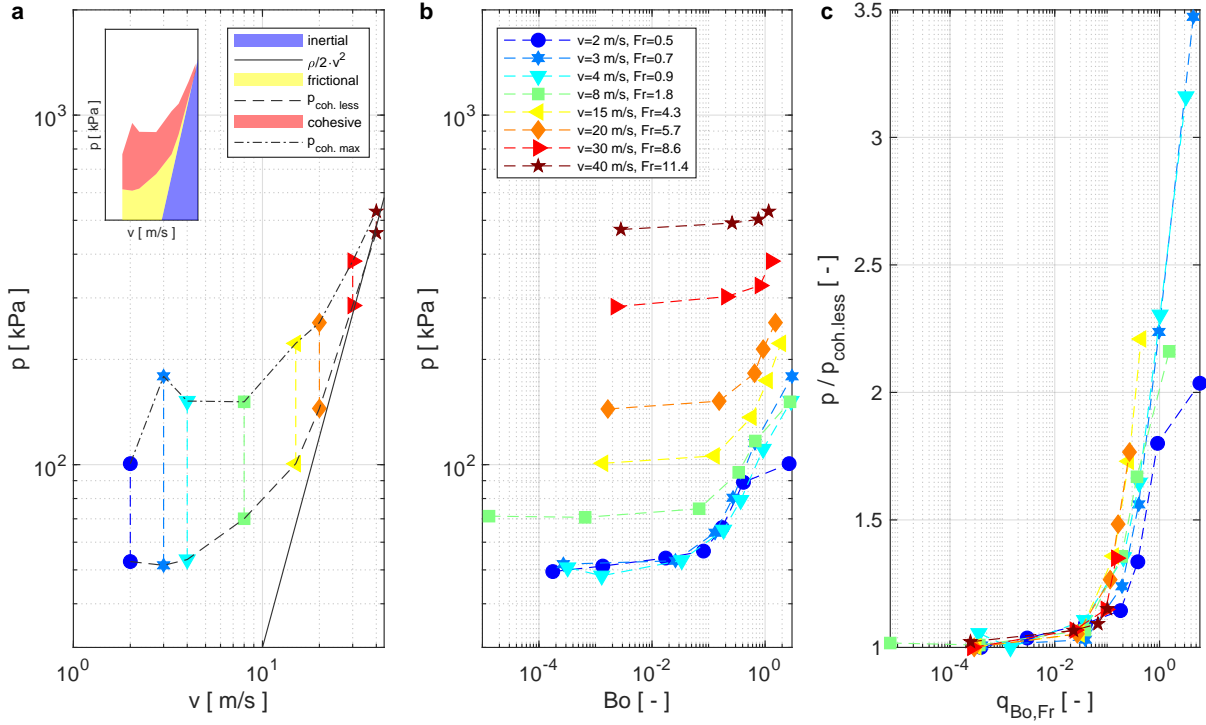


Figure 4. Panel a shows the simulated pressure as a function of velocity with an illustration of the inertial (blue), frictional (yellow) and cohesive (red) pressure contributions in the inset. Panel b shows the simulated pressure for different Fr (colors) as a function of the Bond number. Panel c shows the pressure normalized by the corresponding cohesion-less pressure plotted against the Bond to Froude number ratio $q_{Bo,Fr}$. In panel b and c the dashed interpolating lines between the data points are only a visual aid.

Figure 4b shows the pressure plotted against the Bond number Bo to investigate the influence of cohesive strength on impact pressure. For all Fr values, we observe that at small Bo (equation 2), pressure is a very weak function of Bo . In contrast, we find that for large Bo values the pressure is affected significantly by cohesion (Bo). For increasing velocity, and thus Froude number, the pressure curves are gradually shifted towards higher Bond numbers.

In order to obtain a more universal description of the pressure curves, we compensate for this shift by introducing a new dimensionless number, which is the ratio of the Bond and the Froude number $q_{Bo,Fr} = Bo/Fr$. In Figure 4c, we normalize the absolute pressure p by the impact pressure of the cohesion-less flow $p_{coh.less}$ at the same speed and plot it against $q_{Bo,Fr}$. By normalizing the pressure in this way, we consider only the

pressure increase, which is caused by the presence of cohesion. As Figure 4 c demonstrates, the pressure data collapse almost onto a single curve for the suggested choice of normalization. The curves show that the pressure is amplified by cohesion predominantly for the flows with low velocities. The largest amplifications are observed at 3 m/s and 4 m/s, where the pressure of the cohesive flow is up to 3.5 and 3.2 times higher, respectively, than the pressure of the cohesion-less flow.

3.3 Analysis of the mobilized domain and origin of the pressure amplification at the micro-scale

In order to understand the origin of the pressure amplifications, we analyze the flow around the pylon at the particle level (micro-scale) and compare selected simulations. First, we give a general overview of three scenarios with different velocities and cohesions. In the following subsections 3.3.1 and 3.3.2, we analyze the influence of velocity (Fr) and cohesion (Bo) separately.

We define the mobilized domain as the volume in the flow, where the contact forces between particles adjacent to the obstacle coherently exceed a threshold. With respect to contact forces, we consider only the force component normal to the contact plane. We define this threshold as the median of the contact forces in a control volume around the pylon. In the present analysis, the median of the contact forces is more representative of the undisturbed force level than the mean value because the mean is increased by very high force values in the mobilized domain.

Figure 5 shows the comparison of the mobilized domain for three sample simulations. The first and second rows show simulations of gravitational flows ($Fr = 0.9$) with no and strong cohesion, respectively. The third row shows the simulation of an inertial flow ($Fr = 11.4$) with strong cohesion.

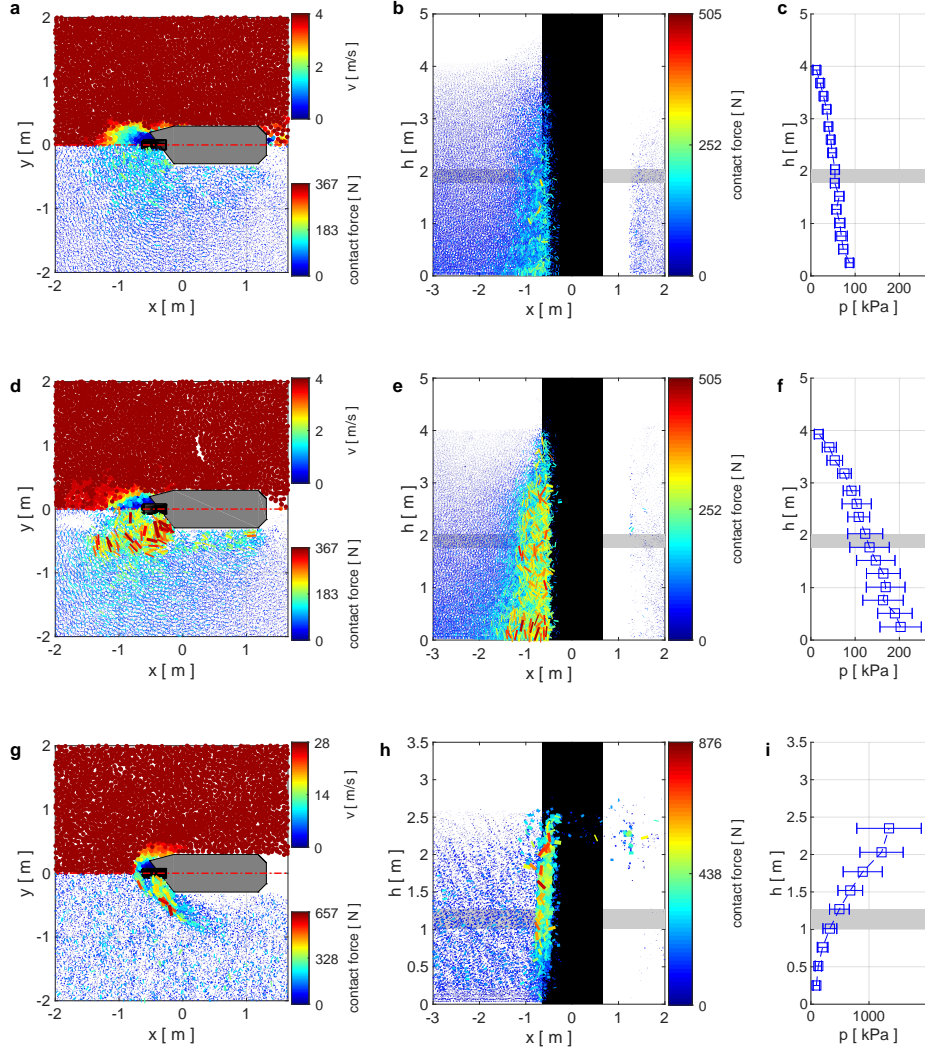


Figure 5. Analysis of the flow and contact forces around the pylon at the micro-scale. Panels a-c show a gravitational flow ($Fr = 0.9$) with no cohesion ($\sigma_{coh} = 0.0$ kPa). Panels d-f show a gravitational flow ($Fr = 0.9$) with high cohesion ($\sigma_{coh} = 10.0$ kPa). Panels g-i show an example of an inertial flow ($Fr = 11.4$) with high cohesion ($\sigma_{coh} = 10.0$ kPa). Panels a, d and g show a horizontal section view through the flow in the middle of the flow height as indicated by the gray area in the other panels. The upper half in Panels a, d and g shows the velocity distribution. The lower half shows inter-particle contact forces whose strength is visualized through the line thickness and color. Panels b, e and h show the vertical section view in x - z plane located in the middle of the pylon (red dash-dotted line in panels a, d and g). The extent of the pylon is visualized by the black area. Panels c, f and i show the impact pressure profiles with the standard deviation of the temporal pressure fluctuations from its mean value indicated by the error bars.

In panels a, d and g we find that force chains stronger than average are only observed in the same region where the velocity of particles is reduced due to the presence of the obstacle. Indeed, the mobilized domains in the velocity field and the contact forces agree well in terms of size and shape.

For the two gravitational examples (first and second rows), the mobilized domain has an almost circular shape and is located upstream of the obstacle. Qualitatively, the contact forces in the mobilized domain away from the pylon increase from top to bottom in both panels b and e in Figure 5. This increase is even more pronounced in the mobilized domain in the vicinity of the obstacle. Not only do the contact forces increase with increasing depth below the surface of the dense flow, but the mobilized domain also grows larger in size. In the simulation with strong cohesion (panel d, $\sigma_{coh} = 10.0$ kPa), the mobilized domain is considerably larger and contact forces are stronger than in the cohesion-less case (panel a, $\sigma_{coh} = 0.0$ kPa).

In the inertial flow (panel g, $\sigma_{coh} = 10.0$ kPa), we observe very strong contact forces only in the vicinity of the obstacle. The shape of the mobilized domain is similar to a bow-wave at the leading edge of the pylon.

When comparing the pressure profiles in panels c and f to the panels b and e, we observe higher pressure at the bottom or for high cohesion, where the mobilized domain and contact forces are larger. Aside, the increase in the pressure itself, pressure fluctuations also increase in the flow with high cohesion. In contrast, for the inertial flow regime (panels h-i), the strongest contact forces and pressures are located at the top where the flow velocity is the highest.

3.3.1 *Influence of the Froude number on the mobilized domain and impact pressure*

In Figure 5, we show that the geometry of the mobilized domain varies in different scenarios. Here we want to examine how the shape changes when varying Froude numbers. To exclude the influence of cohesion we only consider cohesion-less simulations.

Figure 6 a shows the mean contact forces as a function of distance from the obstacle (position 0) and for different Fr (colored symbols). Each point in the plot represents the local contact force averaged in volumes across the whole domain width at varying streamwise positions (x direction). The dotted lines in Figure 6 a indicate the median

of the contact forces in the whole domain, which is used as the threshold for the mobilized domain as defined earlier.

Figure 6 a shows that the shape and location of the mobilized domain change as a function of the Froude number. This is visualized in panels b and c, which display the contact forces for the simulations corresponding to the Froude numbers $Fr = 0.5$ and $Fr = 11.4$, respectively. Similarly to Figure 5, we find a circle-shaped mobilized domain for the lowest Froude number $Fr = 0.5$ (Figure 6 b). Figure 6 c reveals that the mobilized domain is pushed downstream if the Froude number is increased. In this case strong contact forces concentrate just upstream of the obstacle. This leads to the sharp increase in the mean contact force in Figure 6 a for high Fr compared to low Fr .

To quantify the size of the mobilized domain in a single number, we use the standoff distance. Similarly to *Faug* (2015), we define it as the furthest point in the mobilized domain upstream of the obstacle's leading edge. Hence, the standoff distance defined here depends on the choice of the threshold which is used to distinguish between the free flow and the mobilized domain. However, even for a different thresholds, the definition of the mobilized domain with the median force proves to be very robust, and the standoff distance alters only marginally. Here, we use the standoff distance to compare the size of the mobilized domains across all cohesion-less simulations. Figure 6 d shows that the standoff distance decreases dramatically from 1.84 m to approximately 1.0 m with increasing Froude numbers in the range of $0 \leq Fr \leq 5$. For $Fr > 5$, the values of the standoff distance level out at around 0.8 m.

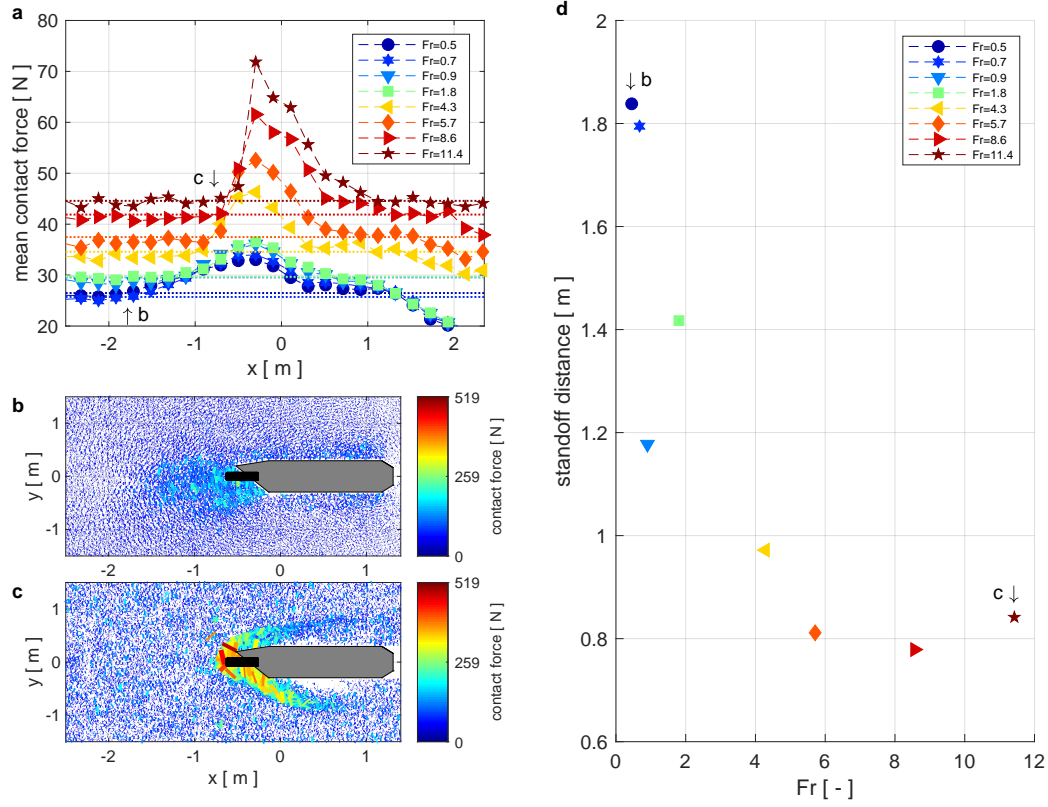


Figure 6. Influence of the Froude number on the mobilized domain and the standoff distance. Panel a shows the mean contact force upstream of the obstacle in streamwise direction for different Froude numbers and $Bo = 0.0$. The dotted lines correspond to the median contact force in simulations with the same color. Panels b and c show horizontal section views at mid-height from the simulation with the lowest and the highest Froude number from panel a, respectively. The lines indicate the force chains whose strength is visualized through the line thickness and color. Panel d shows the standoff distances of the mobilized domain as a function of Fr for cohesionless flows.

3.3.2 Influence of the Bond number on the mobilized domain and impact pressure

In this section we investigate the influence of cohesion on the mobilized domain and the pressure on the obstacle. Similarly to the analysis in the previous section 3.3.1, we consider contact forces to be an indicator of the disturbance of the structure on the flow.

423 However, here we only take contacts directly upstream of the structure into account, be-
 424 cause these are considered the most relevant for pressure build-up. If a larger region in
 425 the y direction is considered, higher forces in the mobilized domain are averaged out and
 426 are therefore less evident. Figure 7 a shows the mean contact forces as a function of stream-
 427 wise location for Bond numbers varying between $Bo = 0.0$ and $Bo = 3.0$. In panel a,
 428 the flow has a Froude number of $Fr = 0.7$. Again we consider the median of the con-
 429 tact forces as an indicator of the overall force level (dotted lines in Figure 7 a).

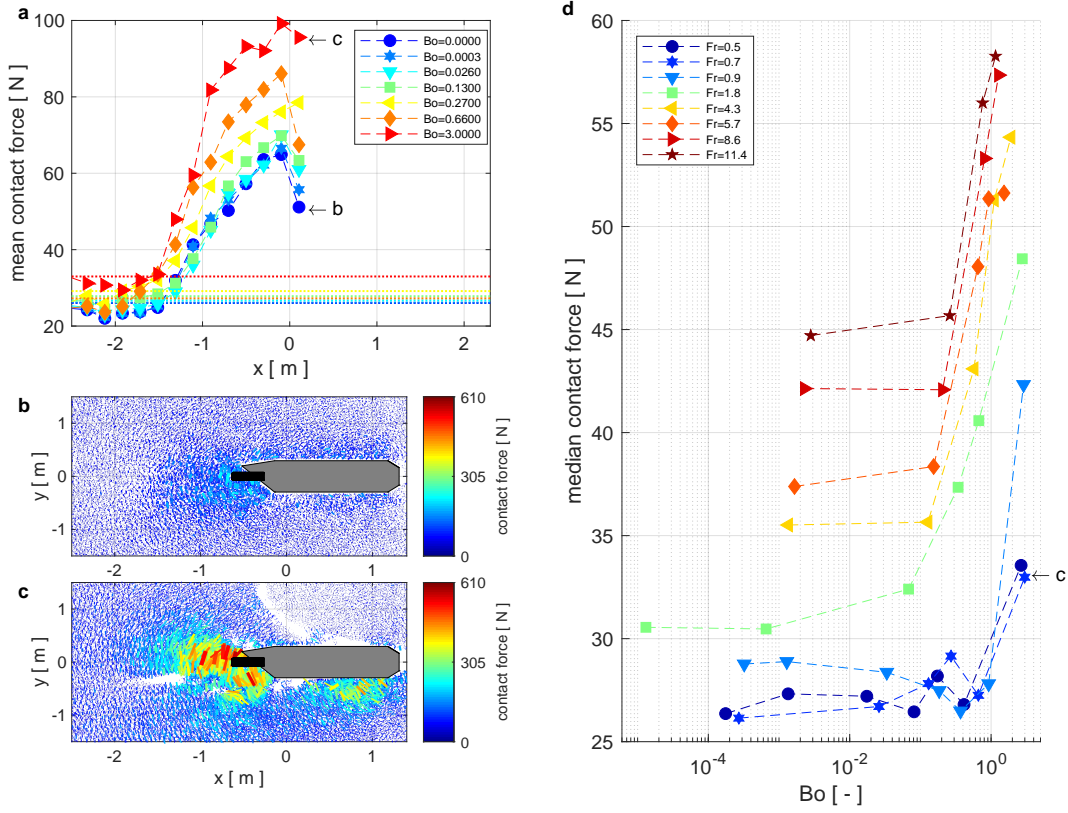


Figure 7. Influence of cohesion on contact forces and the mobilized domain. Panel a shows the mean contact force upstream of the obstacle in streamwise direction for different Bond numbers (different colors and symbols) at $Fr = 0.7$. The dotted lines correspond to the median contact force in simulations with the same color. Panels b and c show horizontal section views at mid-height from the cohesion-less case and the most cohesive simulation from panel a, respectively. The lines indicate the force chains whose strength is visualized through the line thickness and color. Panel d shows the median contact force as a function of Bo , and for different Fr (colors and symbols).

In contrast to Figure 6 a all curves in Figure 7 a have a similar shape. In addition, the standoff distance is almost constant around 1.5 m for all cases, and the dotted lines show that contact forces are enhanced by increasing cohesion. This is even more pronounced for local forces in the mobilized domain just upstream from the obstacle. There, the peak contact forces differ considerably more between low and strong cohesion than

the median contact force. For the example of $Fr = 0.7$ given in Figure 7 a, the peak force (highest red triangle) is approximately 3 times higher than the median of the contact forces (red dotted line) for the highly cohesive case. In the cohesion-less simulation, the peak value (highest dark blue circle) is only 2.5 times higher than the median contact force (dark blue dotted line). A sectional view of the flow around the pylon in the middle of the flow height illustrates this for the case with no cohesion (panel b, $Bo = 0.0$) and strong cohesion (panel c, $Bo = 3.0$). In these two pictures it is obvious that very strong cohesion heavily intensifies contact forces in the vicinity of the obstacle, while the shape and size of the mobilized domain remain largely unchanged. In panel c, the cohesion is so high that the granular material fails along clearly visible fracture lines.

In Figure 7 d, we compare the median contact force of all simulations with varying velocity and cohesion, and plot this as a function of the respective Bond number. Here we find that similarly to the pressure in Figure 4 b, the median contact forces also increase with increasing Fr . Moreover, the median contact forces also exhibit a weak dependency on Bo for low Bo values and a strong dependency for large Bo values.

3.4 Pressure and range of cohesion in gravitational avalanches

As mentioned in section 2.4, we vary cohesion in simulations in the range of 0.0 kPa–20.0 kPa. From Figures 4 c and 7 d we learn that pressure is only amplified by cohesion if a critical threshold of the Bond-to-Froude ratio is exceeded. By comparing simulated to measured pressures of gravitational avalanches, we aim to evaluate which range of cohesive strengths in our simulations can be used to reproduce the pressure values observed in reality. In Figure 8, we show the measurement data of three gravitational avalanches published by *Sovilla et al.* (2010) represented by the gray squares. In these measured warm dense avalanches, velocity ranges from 1 m/s to 8 m/s. The simulated pressure is colored according to the cohesive strength and has different markers for varying velocity. The temporal pressure fluctuations are illustrated by the error bars in panel a, and are separately plotted as a function of the flow height in Figure 8 b for all simulations of panel a.

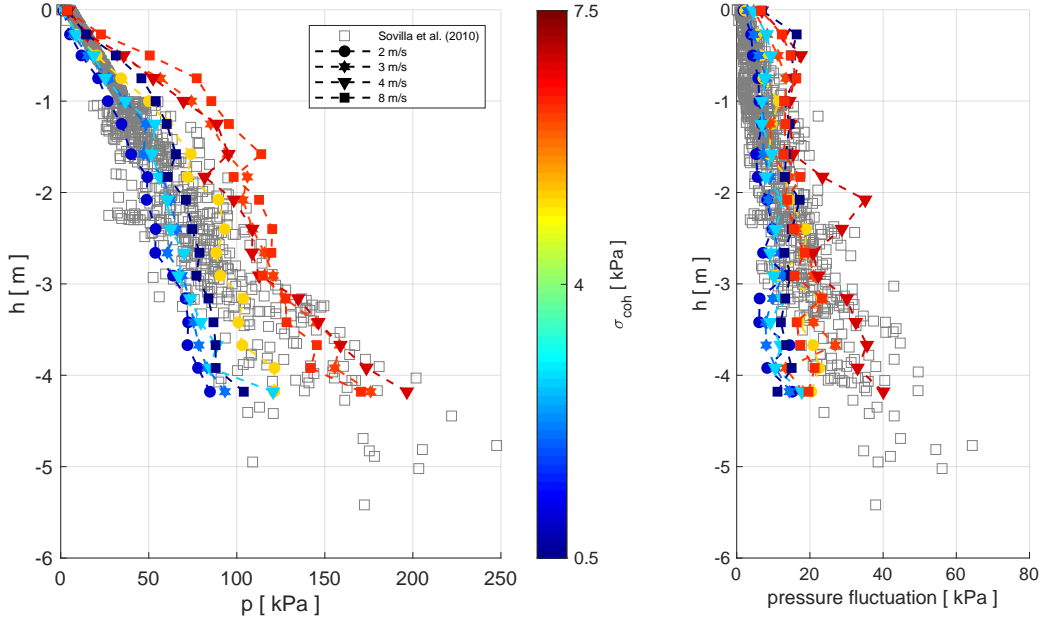


Figure 8. Panel a shows the simulated (colored symbols) and measured (gray squares, from *Sovilla et al. (2010)*) pressure of gravitational avalanches on the VdIS pylon. Panel b shows the pressure fluctuations alone for the same avalanche and simulation data as in panel a.

We find in Figure 8a that cohesive strengths in the range of 0.5 kPa–7.5 kPa fit the measurement data well for the velocity range 2 – 8 m/s. The different symbols indicating velocity in Figure 8a show that avalanche speed has very little influence on the pressure. In contrast, it is apparent from the colors, that flows with less cohesion exert lower pressures than flows with elevated cohesion.

Already in Figure 5, we observed that pressure fluctuations are larger in flows with higher cohesion. This trend is clearly confirmed by Figure 8b. Similar to the measured fluctuations, fluctuations in the simulations also increase with increasing flow depth as well. Although Figure 8b shows good overall agreement between measurements and simulations, the simulated fluctuations are greater than those from measurements at the flow free surface and increase less deeper within the avalanche. Similarly to the pressure itself, fluctuations are smaller and larger in simulations with little and high cohesion, respectively.

4 Discussion

4.1 Modelling avalanche-obstacle interaction with DEM

In section 2, we describe our newly developed DEM model to study the interaction between avalanches and structures. By comparing simulated pressure profiles and full-scale measurements, we show that by treating avalanches as granular flows and applying the Discrete Element Method, the numerical model is able to reproduce flow-depth and velocity squared proportional pressure profiles as well as temporal pressure fluctuations. Furthermore, the simulated pressure values are in the same order as measured values over a wide range of avalanche velocity (Figure 3). Particularly at velocities lower than 5 m/s the simulated impact pressure values agree well with measurements from avalanches # 6236 and # 7226. Only at higher velocities we observe a significant difference between the scattering of the simulated and measured impact pressure. This is probably because we only vary few parameters (Table 1) in our parametric study.

Further limitations of the presented model become apparent due to the differences in pressures and pressure fluctuations between simulations and measurements (Figure 2 and 8). Firstly, the current parallel-bond contact model does not allow for plastic compaction of the granular material. We assume that compaction influences not only pressure at the bottom of the avalanche flow, due to the weight of the snow above, but also across the whole flow height where the snow impacts the obstacle (*Gauer & Jóhannesson, 2009*). Secondly, variation in the radii of particles is small, whereas in natural avalanches, particles are typically larger at the surface of the flow due to particle segregation, which may affect the pressure distribution (*Kern, 2000*).

To obtain a broad understanding of the influence of cohesion in various avalanche scenarios we choose a large range of cohesion ($0.0 \text{ kPa} \leq \sigma_{coh} \leq 20.0 \text{ kPa}$) values and apply it to the whole range of velocities (Table 1). We put these cohesive values into perspective by back calculating the cohesion range from four avalanche measurements. From the calculations and comparisons in sections 3.1 and 3.4, the measurements of these slow avalanches are found to correspond to cohesion values of $0.5 \text{ kPa} \leq \sigma_{coh} \leq 15.6 \text{ kPa}$ in the simulations. Although the back calculated cohesion values agree well with values of tensile strength of snow reported by other authors (*Mellor, 1974; Jamieson & Johnston, 1990; Shapiro et al., 1997; Yamanoi & Endo, 2002*), they are probably only valid for the same choice of the other parameters stated in Table 1.

In this study, we used mechanical snow properties from the literature, which are mostly derived from studies on the mechanics of undisturbed snow. In contrast, avalanche snow may undergo large deformations and transitions (*Steinkogler et al.*, 2015; *Valero et al.*, 2015). Therefore, the stated values must be considered with care in the context of this study. Hence, in the future it would be important to collect data on the mechanical properties of snow granules from avalanches.

The qualitative trend of all results shown in this study have, however, proven to be very robust to changes in any of these parameters. For example, if ρ_p is increased, the absolute pressure value increases as well, but pressure proportionality with flow-depth and velocity squared and the trends shown in sections 3.2, 3.3 and 3.4 remain qualitatively the same. Given this qualitative robustness of the results to changes in the particle properties and because we use a standard cohesive contact model as well as a generic model setup, we believe that the physical understanding gained in this study may also be relevant for similar processes, where cohesive granular flows interact with rigid structures.

4.2 Impact pressure contributions at the macro-scale

In the inset of Figure 4 a, we visualize and highlight the inertial, frictional and cohesive impact pressure contributions. The complex interplay between these contributions in avalanche dynamics are investigated for the first time in this study. It is important to note that all three contributions are present for the whole range of Fr , but with changing importance as a share of the entire impact pressure.

The inertial contribution is known from other fields (e.g. fluid dynamics, granular flows) and is proportional to density and velocity squared. This v^2 proportionality is confirmed by the slope of the dashed black line in Figure 4 a, which is ~ 2 for high velocities ($v \gtrsim 20$ m/s). Hence, we confirm that avalanche pressure is governed primarily by inertial impact for Froude numbers close to or greater than 10 (*Voellmy*, 1955; *Thibert et al.*, 2008; *Faug*, 2015).

The frictional contribution is most pronounced at low Fr and arises due to the granular nature of the flow. It is, therefore, also present in cohesion-less granular flows (*Chehata et al.*, 2003; *Albert et al.*, 2001). Thus, even a hypothetical cohesion-less avalanche would exert considerably higher pressures on an obstacle at low Fr , compared to the inertial contribution alone.

The cohesive contribution is also highest at low Fr and constitutes up to 70 % of the entire impact pressure for the range of cohesion from Table 1. If we consider the range of back calculated cohesion ($0.5 \text{ kPa} \leq \sigma_{coh} \leq 15.6 \text{ kPa}$) the largest pressure amplification factor due to cohesion is 2.1 with respect to the cohesion-less case. Furthermore, we show that cohesion is only relevant for a pressure increase above a certain threshold, where the slopes of the curves in Figure 4 b increase dramatically. The idea of a critical cohesion threshold is also supported by other studies (*Favier et al.*, 2013; *Steinkogler et al.*, 2015). Most likely, below this threshold the flow behaves similarly to a cohesion-less flow as long as collisional forces are strong enough to break the cohesive bonds between particles. If the cohesive strength is above this threshold value, the bonds cannot be broken anymore by the collisional forces. Thus, the flow exhibits a cohesive behavior (section 3.3.2) and impact pressure is amplified.

Because the cohesion threshold is included in the range of the back calculated cohesion values we assume that real avalanches are most likely subject to this transition between cohesive and nearly cohesion-less flow behavior. Similarly to the sharp transition of granulation behavior at the threshold temperature -1°C reported by *Steinkogler et al.* (2015), we demonstrate that also here small changes in cohesion around the cohesion threshold, above which pressure is amplified, may lead to substantial changes in pressure.

We also observe that the cohesion threshold varies with Fr and assume that this is due to the competing effect of cohesive and inertial forces in the snow. We take this into account by defining the Bond to Froude ratio $q_{Bo,Fr}$. Moreover, we decouple the cohesive pressure contribution from the frictional and inertial contribution by normalizing the impact pressure of a cohesive flow with the cohesion-less pressure. The collapse of the data from Figure 4 b onto a single curve in Figure 4 c shows that we find a scaling for the impact pressure of a cohesive granular as a function of the cohesion-less pressure as well as Bo and Fr . This scaling allows us to estimate the impact pressure of a cohesive granular flow by calculating the pressure of cohesion-less flow and multiplying by the factor given in the curve in Figure 4 c. This is expedient because the problem of cohesion-less granular flow impacting an obstacle has been studied in the past (e.g. *Albert et al.*, 2001).

4.3 Micro-scale processes of impact pressure build-up

In this study, we confirm the existence of the mobilized domain postulated by *Faug* (2015), even in cohesion-less granular flows. Hence, the mobilized domain owes its presence to the granular nature and the force chains in the granular flow, rather than the presence of cohesion. Consequently, the mobilized domain in cohesion-less flows is most likely the origin of the frictional pressure contribution (yellow area in inset of Figure 4 a).

Our results show that the shape of the mobilized domain can be described using the Froude number only. For low Fr , the domain has an approximately circular shape and is located mainly upstream of the obstacle (Figure 6 b). If the Froude number is increased, the mobilized domain is “pushed” gradually downstream by the flow. For the highest Froude numbers, the mobilized domain has the shape of a bow wave (Figure 6 c).

Here, we use the standoff distance (section 3.3.1) to characterize the extent of the mobilized domain. Figure 6 d shows that for increasing Fr , the standoff distance decreases dramatically from a maximum of ~ 2.0 m in the range of $Fr < 5$, and then levels out at around 1 m for $Fr > 5$. This result agrees qualitatively with the findings of *Cui & Gray* (2013) and *Faug et al.* (2002) on the standoff distance of granular bow shocks and size of mobilized domains, respectively. Interestingly, a similar dependency is found experimentally between the drag coefficient of a wall and Fr in a mud flow by *Tiberghien et al.* (2007), as well as for the hydrodynamic impact pressure of debris flows and Fr by *Proske et al.* (2011). Quantitatively, however, the maximum standoff distance in all simulations is considerably smaller than the 3.5 m–7.0 m estimated by *Sovilla et al.* (2016) using the theory of *Faug* (2015) for the same structure. Furthermore, it is important to bear in mind that the size of the mobilized domain and therefore the standoff distance probably differs substantially for other geometries.

We also show that cohesion neither influences the size, nor shape of the mobilized domain, but changes the level of the contact forces inside the domain. As a general rule, we observe that the median contact forces increase with increasing cohesion. Our results confirm the observations of *Favier et al.* (2013), who found that cohesion increase leads to a densification of the contact network and to an increase in the temporal contact persistency. Figure 7 d shows that the dependency of the median contact force and cohesion is not linear. Indeed, the median of the contact forces are almost constant for low Bond numbers but increase sharply if a particular Bo is exceeded. The resemblance of Figure 4 b

to Figure 7d clearly indicates that the pressure increase due to cohesion at the macro-scale is directly linked to the intensified contact forces at the micro-scale.

While further proof is needed, we assume that the frictional and cohesive contributions observed at the macro-scale can be linked to processes at the particle scale. The frictional contribution arises due to the frictional behaviour between particles, which causes the mobilised domain to form around a structure due to jamming or building of force chains. Thereby, the force of the incoming flow probably acts on the larger apparent surface of the obstacle, which is the outline of the mobilized domain, and it is transmitted and concentrated at the obstacle surface through the force chains. By increasing the cohesion between particles, the force transmission from the apparent surface to the obstacle is enhanced, and results in higher pressure on the obstacle surface.

5 Conclusions

In this study we present a newly developed DEM model to investigate the interaction between dense snow avalanches and obstacles. We show that the model is able to reproduce the pressure profiles and the range of temporal pressure fluctuations exerted by avalanches on the VdlS pylon for a wide range of Froude numbers and cohesion values. This indicates that approximating avalanches as granular flows and applying DEM allows us to capture the most important physical processes involved in avalanche-obstacle interaction.

We also identify, however, some limitations of the model. Firstly, the contact model does not allow for compaction of snow, and particle segregation cannot occur because the particles are not flowing freely. Secondly, particle properties are estimated from values found in the literature, which are based on the mechanical behaviour of undisturbed snow samples. Hence, to obtain relevant results in future investigations on the mechanical properties and contact behavior of snow avalanche granules will be needed.

In our study we identify three pressure contributions, which are of varying importance depending on avalanche speed. The inertial contribution, which is proportional to velocity squared and density, is most important at high avalanche velocities. The frictional contribution arises due to the granular nature of the flow and is therefore inherently present in cohesion-less flows. Hence, depending on the granulometry, the impact pressure of slow avalanches is increased by this frictional contribution even without the presence of cohesion, such as in cold avalanches. In agreement with previous studies, we

find growing evidence that the formation of force chains and the existence of a mobilized domain around the structure in cohesion-less flows are factors leading to elevated pressures at low Fr compared to the impact pressure in Newtonian fluids (*Sovilla et al.*, 2010; *Favier et al.*, 2013; *Faug*, 2015). The shape of this mobilized domain smoothly changes from a nearly circular shape upstream of the obstacle for low Fr , into a bow-wave-like shape for high Fr .

The cohesive contribution increases the impact pressure of a cohesion-less flow by a maximum factor of 2.1 if a critical cohesion value is exceeded, such as in warm avalanches. We find that this increase of impact pressure is caused by the amplification of contact forces within the entire cohesive flow, but especially within the boundaries of the mobilized domain. Surprisingly, the shape and size of the domain are barely influenced by cohesion as assumed in other studies (*Faug*, 2015; *Rognon et al.*, 2008).

Furthermore, we find a scaling relating the pressure of cohesive and cohesion-less flows. This allows us to reduce the problem of calculating the pressure of a cohesive granular flow, to calculating the pressure of a cohesion-less flow, which has been investigated in the past (*Albert et al.*, 2001; *Calvetti et al.*, 2017; *Albaba et al.*, 2015; *Moriguchi et al.*, 2009; *Chanut et al.*, 2009).

Thanks to the identification of the three pressure contributions at the macro-scale and the underlying processes at the particle level, this study contributes to our understanding of the build-up of impact pressure of cohesive granular flows on narrow structures. Finally, as we use a standard cohesive bond contact model and the qualitative results are not affected by changes of the properties of the granular material, we are convinced that this study may not only be relevant for snow avalanches, but for the interaction of structures and flows of cohesive granular materials in general.

Acknowledgments

Michael Kyburz, Betty Sovilla and Christophe Ancey acknowledge the Swiss National Science Foundation for funding this project “Pressure on obstacles induced by granular snow avalanches” (grant no. 200021_169640). Johan Gaume acknowledges financial support from the Swiss National Science Foundation (grant no. PCEFP2_181227). The supporting information and the code to be used with the Itasca PFC3D software to reproduce the data presented in this paper is available in the open access data repository Zenodo, which is financed by the Horizon 2020 project OpenAIRE and hosted by CERN. The associated entry can be accessed via Kyburz M. L., Sovilla, B., Gaume J., & An-

cey C. (2019). Decoupling the role of inertia, friction and cohesion in dense granular avalanche pressure build-up on obstacles [Supporting Information]. Zenodo. <https://doi.org/10.5281/zenodo.3239031>. We would like to thank the Editor Ton Hoitink, the Associate Editor Michele Bolla Pit-taluga, as well as Thierry Faug and two anonymous reviewers for their helpful comments.

References

- Albaba, A., S. Lambert, F. Nicot, and B. Chareyre (2015), Relation between microstructure and loading applied by a granular flow to a rigid wall using DEM modeling, *Granular Matter*, *17*(5), 603–616, <https://doi.org/10.1007/s10035-015-0579-8>.
- Albert, I., J. G. Sample, A. J. Morss, S. Rajagopalan, A.-L. Barabási, and P. Schiffer (2001), Granular drag on a discrete object: Shape effects on jamming, *Physical Review E*, *64*, 061,303, <https://doi.org/10.1103/PhysRevE.64.061303>.
- Albert, R., M. Pfeifer, A.-L. Barabasi, and P. Schiffer (1999), Slow drag in a granular medium, *Physical Review Letters*, *82*, 205–208, <https://doi.org/10.1103/PhysRevLett.82.205>.
- Ammann, W. J. (1999), A new Swiss test-site for avalanche experiments in the Vallée de la Sionne/Valais, *Cold Regions Science and Technology*, *30*(1), 3–11, [https://doi.org/10.1016/S0165-232X\(99\)00010-5](https://doi.org/10.1016/S0165-232X(99)00010-5).
- Ancey, C., and V. Bain (2015), Dynamics of glide avalanches and snow gliding, *Reviews of Geophysics*, *53*(3), 745–784, <https://doi.org/10.1002/2015RG000491>.
- Baroudi, D., and E. Thibert (2009), An instrumented structure to measure avalanche impact pressure: Error analysis from monte carlo simulations, *Cold Regions Science and Technology*, *59*(2), 242 – 250, <https://doi.org/10.1016/j.coldregions.2009.05.010>, international Snow Science Workshop (ISSW) 2008.
- Bartelt, P., and B. W. McArdell (2009), Granulometric investigations of snow avalanches, *Journal of Glaciology*, *55*(193), 829833, <https://doi.org/10.3189/002214309790152384>.
- Burkard, A., H. U. Gubler, and B. W. Salm (1990), *Berechnung von Fliesslawinen: eine Anleitung für Praktiker mit Beispielen, Mitteilungen des Eidgenössischen Instituts für Schnee- und Lawinenforschung*, vol. 47, Eidgenössisches Institut für Schnee- und Lawinenforschung, Davos.

- Calvetti, F., C. G. di Prisco, and E. Vairaktaris (2017), DEM assessment of impact forces of dry granular masses on rigid barriers, *Acta Geotechnica*, *12*(1), 129–144, <https://doi.org/10.1007/s11440-016-0434-z>.
- Chanut, B., T. Faug, and M. Naaim (2009), Mean force on a wall overflowed by dense granular avalanches: Discrete Numerical Simulations, *AIP Conference Proceedings*, *1145*(1), 609–612, <https://doi.org/10.1063/1.3180000>.
- Chehata, D., R. Zenit, and C. R. Wassgren (2003), Dense granular flow around an immersed cylinder, *Physics of Fluids*, *15*(6), 1622–1631, <https://doi.org/10.1063/1.1571826>.
- Cui, X., and J. M. N. T. Gray (2013), Gravity-driven granular free-surface flow around a circular cylinder, *Journal of Fluid Mechanics*, *720*, 314337, <https://doi.org/10.1017/jfm.2013.42>.
- Cundall, P. A., and O. D. L. Strack (1979), A discrete numerical model for granular assemblies, *Géotechnique*, *29*(1), 47–65, <https://doi.org/10.1680/geot.1979.29.1.47>.
- Faug, T. (2015), Macroscopic force experienced by extended objects in granular flows over a very broad froude-number range, *The European Physical Journal E*, *38*(5), 34, <https://doi.org/10.1140/epje/i2015-15034-3>.
- Faug, T., P. Lachamp, and M. Naaim (2002), Experimental investigation on steady granular flows interacting with an obstacle down an inclined channel: study of the dead zone upstream from the obstacle. Application to interaction between dense snow avalanches and defence structures, *Natural Hazards and Earth System Science*, *2*(3/4), 187–191, <https://doi.org/10.5194/nhess-2-187-2002>.
- Favier, L., D. Daudon, and F.-V. Donzé (2013), Rigid obstacle impacted by a supercritical cohesive granular flow using a 3d discrete element model, *Cold Regions Science and Technology*, *85*, 232 – 241, <https://doi.org/10.1016/j.coldregions.2012.09.010>.
- Fischer, J.-T., R. Kaitna, K. Heil, and I. Reiweiger (2018), The heat of the flow: Thermal equilibrium in gravitational mass flows, *Geophysical Research Letters*, *45*(20), 11,219–11,226, <https://doi.org/10.1029/2018GL079585>.
- Gauer, P., and T. Jóhannesson (2009), The design of avalanche protection dams Recent practical and theoretical developments, chap. Loads on walls, pp. 77–94, Climate Change and Environmental Risks, EUROPEAN COMMISSION.

- Gauer, P., and K. Kristensen (2016), Four decades of observations from NGI's full-scale avalanche test site Ryggfonn – Summary of experimental results, *Cold Regions Science and Technology*, 125, 162 – 176, <https://doi.org/10.1016/j.coldregions.2016.02.009>.
- Gaume, J., G. Chambon, N. Eckert, M. Naaim, and J. Schweizer (2015a), Influence of weak layer heterogeneity and slab properties on slab tensile failure propensity and avalanche release area, *The Cryosphere*, 9(2), 795–804, <https://doi.org/10.5194/tc-9-795-2015>.
- Gaume, J., A. van Herwijnen, G. Chambon, K. W. Birkeland, and J. Schweizer (2015b), Modeling of crack propagation in weak snowpack layers using the discrete element method, *The Cryosphere*, 9(5), 1915–1932, <https://doi.org/10.5194/tc-9-1915-2015>.
- Gaume, J., T. Gast, J. Teran, A. van Herwijnen, and C. Jiang (2018), Dynamic anticrack propagation in snow, *Nature communications*, 9(1), 3047, <https://doi.org/10.1038/s41467-018-05181-w>.
- Gerling, B., H. Löwe, and A. van Herwijnen (2017), Measuring the Elastic Modulus of Snow, *Geophysical Research Letters*, 44(21), 11,088–11,096, <https://doi.org/10.1002/2017GL075110>, 2017GL075110.
- Hauksson, S., M. Pagliardi, M. Barbolini, and T. Jóhannesson (2007), Laboratory measurements of impact forces of supercritical granular flow against mast-like obstacles, *Cold Regions Science and Technology*, 49(1), 54 – 63, <https://doi.org/10.1016/j.coldregions.2007.01.007>, selected Papers from the General Assembly of the European Geosciences Union (EGU), Vienna, Austria, 25 April 2005.
- Jamieson, J., and C. Johnston (1990), In-situ tensile tests of snow-pack layers, *Journal of Glaciology*, 36(122), 102–106, <https://doi.org/10.3189/S002214300000561X>.
- Kern, M. (2000), *Inverse grading in granular flow*, 336 pp., EPFL, Lausanne.
- Kern, M., P. Bartelt, B. Sovilla, and O. Buser (2009), Measured shear rates in large dry and wet snow avalanches, *Journal of Glaciology*, 55(190), 327–338, <https://doi.org/10.3189/002214309788608714>.
- Kern, M. A., P. A. Bartelt, and B. Sovilla (2010), Velocity profile inversion in dense avalanche flow, *Annals of Glaciology*, 51(54), 27–31, <https://doi.org/10.3189/172756410791386643>.

- Köhler, A., J. McElwaine, and B. Sovilla (2018a), GEODAR data and the flow regimes of snow avalanches, *Journal of Geophysical Research: Earth Surface*, *0*(0), <https://doi.org/10.1002/2017JF004375>.
- Köhler, A., J.-T. Fischer, R. Scandroglio, M. Bavay, J. McElwaine, and B. Sovilla (2018b), Cold-to-warm flow regime transition in snow avalanches, *The Cryosphere*, *12*, 3759–3774, <https://doi.org/10.5194/tc-12-3759-2018>.
- Mellor, M. (1968), Avalanches, *Crrrel Research Reports, Army Dept/US/*.
- Mellor, M. (1974), *A review of basic snow mechanics*, US Army Cold Regions Research and Engineering Laboratory.
- Moriguchi, S., R. I. Borja, A. Yashima, and K. Sawada (2009), Estimating the impact force generated by granular flow on a rigid obstruction, *Acta Geotechnica*, *4*(1), 57–71, <https://doi.org/10.1007/s11440-009-0084-5>.
- Platzter, K., P. Bartelt, and M. Kern (2007), Measurements of dense snow avalanche basal shear to normal stress ratios (S/N), *Geophysical Research Letters*, *34*(7), L07,501, <https://doi.org/10.1029/2006GL028670>.
- Potyondy, D., and P. Cundall (2004), A bonded-particle model for rock, *International Journal of Rock Mechanics and Mining Sciences*, *41*(8), 1329 – 1364, <https://doi.org/10.1016/j.ijrmms.2004.09.011>, rock Mechanics Results from the Underground Research Laboratory, Canada.
- Proske, D., J. Suda, and J. Hübl (2011), Debris flow impact estimation for breakers, *Georisk: Assessment and Management of Risk for Engineered Systems and Geohazards*, *5*(2), 143–155, <https://doi.org/10.1080/17499518.2010.516227>.
- Rognon, P. G., J.-N. Roux, M. Naaïm, and F. Chevoir (2008), Dense flows of cohesive granular materials, *Journal of Fluid Mechanics*, *596*, 21–47, <https://doi.org/10.1017/S0022112007009329>.
- Roy, S., S. Luding, and T. Weinhart (2017), A general(ized) local rheology for wet granular materials, *New Journal of Physics*, *19*(4), 043,014, <https://doi.org/10.1088/1367-2630/aa6141>.
- Salm, B. (1964), Anlage zur untersuchung dynamischer wirkungen von bewegtem schnee, *Zeitschrift für angewandte Mathematik und Physik ZAMP*, *15*(4), 357–375, <https://doi.org/10.1007/BF01601287>.
- Salm, B. (1966), Contribution to avalanche dynamics, *Scientific Aspects of Snow and Ice Avalanche*, *69*, 199214.

- Scapozza, C. (2004), Entwicklung eines dichte-und temperaturabhängigen Stoffgesetzes zur Beschreibung des visko-elastischen Verhaltens von Schnee, Phdthesis, ETH Zürich, <https://doi.org/10.3929/ethz-a-004680249>.
- Shapiro, L. H., J. Johnson, M. Sturm, and G. Blaisdell (1997), Snow mechanics: Review of the state of knowledge and applications, *CRREL Report 97-3*, p. 40.
- Sovilla, B., M. Schaer, M. Kern, and P. Bartelt (2008a), Impact pressures and flow regimes in dense snow avalanches observed at the valle de la sionne test site, *Journal of Geophysical Research: Earth Surface*, *113*(F1), <https://doi.org/10.1029/2006JF000688>.
- Sovilla, B., M. Schaer, and L. Rammer (2008b), Measurements and analysis of full-scale avalanche impact pressure at the valle de la sionne test site, *Cold Regions Science and Technology*, *51*(2), 122 – 137, <https://doi.org/10.1016/j.coldregions.2007.05.006>, international Snow Science Workshop (ISSW) 2006.
- Sovilla, B., M. Kern, and M. Schaer (2010), Slow drag in wet-snow avalanche flow, *Journal of Glaciology*, *56*(198), 587–592, <https://doi.org/10.3189/002214310793146287>.
- Sovilla, B., S. Margreth, M. Schaer, and C. Ancey (2014), Taking into account wet avalanche load for the design of pylon-like structures., *Proceedings of International Snow Science - Montana State University Library*, pp. 727–732.
- Sovilla, B., T. Faug, A. Köhler, D. Baroudi, J.-T. Fischer, and E. Thibert (2016), Gravitational wet avalanche pressure on pylon-like structures, *Cold Regions Science and Technology*, *126*(Supplement C), 66 – 75, <https://doi.org/10.1016/j.coldregions.2016.03.002>.
- Steinkogler, W., J. Gaume, H. Löwe, B. Sovilla, and M. Lehning (2015), Granulation of snow: From tumbler experiments to discrete element simulations, *Journal of Geophysical Research: Earth Surface*, *120*(6), 1107–1126, <https://doi.org/10.1002/2014JF003294>, 2014JF003294.
- Teufelsbauer, H., Y. Wang, S. P. Pudasaini, R. I. Borja, and W. Wu (2011), DEM simulation of impact force exerted by granular flow on rigid structures, *Acta Geotechnica*, *6*(3), 119, <https://doi.org/10.1007/s11440-011-0140-9>.
- Thibert, E., D. Baroudi, A. Limam, and P. Berthet-Rambaud (2008), Avalanche impact pressure on an instrumented structure, *Cold Regions Science and Technology*, *54*(3), 206 – 215, <https://doi.org/10.1016/j.coldregions.2008.01.005>, snow

829 avalanche formation and dynamics.

- 830 Thibert, E., H. Bellot, X. Ravanat, F. Ousset, G. Pulfer, M. Naaïm, P. Hagen-
 831 muller, F. Naaïm-Bouvet, T. Faug, K. Nishimura, Y. Ito, D. Baroudi, A. Prokop,
 832 P. Schön, A. Soruco, C. Vincent, A. Limam, and R. Héno (2015), The full-scale
 833 avalanche test-site at lautaret pass (french alps), *Cold Regions Science and Tech-*
 834 *nology*, 115, 30 – 41, <https://doi.org/10.1016/j.coldregions.2015.03.005>.
- 835 Tiberghien, D., D. Laigle, M. Naaïm, E. Thibert, and F. Ousset (2007), Experimen-
 836 tal investigations of interaction between mudflow and an obstacle, *Debris-flow*
 837 *hazards mitigation: mechanics, prediction, and assessment*, pp. 281–292.
- 838 Valero, C. V., K. W. Jones, Y. Bühler, and P. Bartelt (2015), Release temperature,
 839 snow-cover entrainment and the thermal flow regime of snow avalanches, *Journal*
 840 *of Glaciology*, 61(225), 173184, <https://doi.org/10.3189/2015JoG14J117>.
- 841 Voellmy, A. (1955), Über die Zerstörungskraft von Lawinen (On the destructive
 842 forces of avalanches), *Schweizerische Bauzeitung*, 73(12/15/17/19), 159–162, 212–
 843 217, 246–249, 280–285, <http://doi.org/10.5169/seals-61891>.
- 844 Wieghardt, K. (1975), Experiments in granular flow, *Annual Review of Fluid Me-*
 845 *chanics*, 7(1), 89–114, <https://doi.org/10.1146/annurev.fl.07.010175.000513>.
- 846 Yamanoi, K., and Y. Endo (2002), Dependence of shear strength of snow cover on
 847 density and water content, *Seppyo*, 64(4), 443–451, <https://doi.org/10.5331/seppyo.64.443>.
- 848